

## Cloud Water Resource in North China in 2017 Simulated by the CMA-CPEFS Cloud Resolving Model: Validation and Quantification

Chao TAN, Miao CAI, Yuquan ZHOU\*, Weiguo LIU, and Zhijin HU

CMA Key Laboratory for Cloud Physics, Weather Modification Center, China Meteorological Administration (CMA), Beijing 100081

(Received June 23, 2021; in final form January 11, 2022)

### ABSTRACT

Based on the concept of cloud water resource (CWR) and the cloud microphysical scheme developed by the Chinese Academy of Meteorological Sciences (CAMS), a coupled mesoscale and cloud-resolving model system is developed in the study for CWR numerical quantification (CWR-NQ) in North China for 2017. The results show that (1) the model system is stable and capable for performing 1-yr continuous simulation with a water budget error of less than 0.2%, which indicates a good water balance. (2) Compared with the observational data, it is confirmed that the simulating capability of the CWR-NQ approach is decent for the spatial distribution of yearly cumulative precipitation, daily precipitation intensity, yearly average spatial distribution of water vapor. (3) Compared with the CWR diagnostic quantification (CWR-DQ), the results from the CWR-NQ differ mainly in cloud condensation and cloud evaporation. However, the deviation of the net condensation (condensation minus evaporation) between the two methods is less than 1%. For other composition variables, such as water vapor advection, surface evaporation, precipitation, cloud condensation, and total atmospheric water substances, the relative differences between the CWR-NQ and the CWR-DQ are less than 5%. (4) The spatiotemporal features of the CWR in North China are also studied. The positive correlation between water vapor convergence and precipitation on monthly and seasonal scales, and the lag of precipitation relative to water vapor convergence on hourly and daily scales are analyzed in detail, indicating the significance of the state term on hourly and daily scales. The effects of different spatial scales on the state term, advection term, source-sink term, and total amount are analyzed. It is shown that the advective term varies greatly at different spatiotemporal scales, which leads to differences at different spatiotemporal scales in CWR and related characteristic quantities.

**Key words:** cloud water resource, atmospheric moisture budget, long-term continuous simulation, model validation, spatiotemporal characteristics

**Citation:** Tan, C., M. Cai, Y. Q. Zhou, et al., 2022: Cloud water resource in North China in 2017 simulated by the CMA-CPEFS cloud resolving model: Validation and quantification. *J. Meteor. Res.*, **36**(3), 520–538, doi: 10.1007/s13351-022-1118-2.

### 1. Introduction

Atmospheric water substances include water vapor and solid and liquid hydrometeors (collectively called atmospheric hydrometeors). The precipitation is formed when atmospheric hydrometeors fall to the ground, and it requires complex dynamic and microphysical processes (Ramanathan et al., 1989). The precipitation is not a direct product of atmospheric water vapor, and it needs condensation processes of water vapor to liquid and solid hydrometeors. Precipitation is the primary source of surface water resources, providing and supplementing soil

moisture, groundwater, snow cover, glaciers, and surface runoff (Mason, 1971; Pruppacher and Klett, 1978). Since the 1990s, water resource shortage has become one of the critical factors limiting social and economic development due to global climate change, economic and social development, population increase, and ecological environment deterioration. Therefore, it is of great strategic importance to understand the status and change trend of the cloud water resource (CWR) and develop CWR scientifically and reasonably, in order to effectively alleviate water scarcity, protect the ecological environment, and guarantee the sustainable development of society and

Supported by the National Key Research and Development Program of China (2016YFA0601701), National Natural Science Foundation of China (42075191), and National High Technology Research and Development Program of China (2012AA120902).

\*Corresponding author: zhouyq@cma.gov.cn

© The Chinese Meteorological Society and Springer-Verlag Berlin Heidelberg 2022

economy.

[Zhou et al. \(2020\)](#) defined 16 CWR composition variables and 12 CWR characteristic quantities based on atmospheric water substance balance equations. The 16 CWR composition variables include the initial and final values, influx and outflux of atmospheric hydrometeors and water vapor, cloud condensation, cloud evaporation, surface evaporation, and precipitation. Based on 16 composition variables, it is possible to quantify the CWR and related characteristic quantities, such as total atmospheric water substances, conversion efficiency, mean mass, and renewal time.

The CWR diagnostic quantification (CWR-DQ) and CWR numerical quantification (CWR-NQ) are essential methods for assessing regional CWR. For the CWR-DQ methods, the calculations of atmospheric water substance state terms and fluxes require the observation of vertical cloud fields. However, due to the complexity of cloud structure, it is difficult to obtain complete and continuous observations of three-dimensional cloud fields, although there are many observation means. The observation by aircraft through clouds is the most straightforward method, but can only obtain macro and micro information of clouds along the flight track during the observed period ([Hobbs et al., 1980](#)). Some ground-based remote sensing instruments including cloud radar, laser ceilometer, and microwave radiometer can be used to retrieve continuous observations of cloud structure, cloud base height, and cloud liquid water path at specific locations ([Zhao et al., 2012](#)). In different regions of China such as Northwest China, Northeast China, the Tibetan Plateau, North China, and South China, [Zhao et al. \(2019\)](#) analyzed the cloud macro- and microphysical characteristics by the 15-yr Moderate Resolution Imaging Spectroradiometer (MODIS) Level-3 data, including cloud volume, cloud-top pressure, cloud-top temperature, cloud optical thickness, and effective particle radius. Based on *Himawari-8* satellite cloud products from July 2015 to June 2016, [Yang et al. \(2020\)](#) studied the spatiotemporal characteristics of clouds, including cloud-top height and cloud-top temperature, in Northwest China, North China, Southeast China, and the Tibetan Plateau. But the CWR calculation should take into account the physical variables such as condensation and evaporation caused by the phase transformation between water vapor and atmospheric hydrometeors, while these variables cannot be obtained directly from observations and have to be calculated from balance equation. The two methods, CWR-DQ and CWR-NQ, complement and corroborate each other in order to obtain more complete and reasonable fine quantitative results of the CWR ([Cai](#)

[et al., 2020](#)).

The difficulty of the CWR-NQ lies in coupling the computational methods of the CWR and related physical variables with microphysical schemes in mesoscale models ([Cai et al., 2020](#)). In addition, if the atmospheric water substances are conserved in the model during long-term continuous simulation, the errors between simulations and observations are acceptable, and the scale at which the CWR discussed and studied can be extended from daily to monthly and yearly are important for the credibility of numerical simulation results ([Zhou et al., 2020](#)).

Based on numerical models, previous studies on water balance have been carried out from weather and climate perspectives. In terms of climate model research, [Song et al. \(2013\)](#) simulated the summer water vapor transport in the Asia-Pacific monsoon region by using the Community Earth System Model (CESM), and they compared the model results with NCEP data and results from 22 coupled air-sea circulation models. The comparison results showed that most of the models performed well on simulating the spatial characteristics of the water vapor transport, and thus, a detailed study on water vapor transport was carried out on a global scale. However, this study did not cover the transport characteristics of atmospheric hydrometeors. [Jiang et al. \(2012\)](#) simulated column cloud water content by the Coupled Model Intercomparison Project phase 5 (CMIP5) model ensemble and examined it against NASA A-Train satellite data. The results indicated that both column cloud water content and water vapor content simulated by the CMIP5 differed significantly from observations due to the coarse model resolution. Therefore, it is difficult to accurately characterize the detailed hydrometeors by simple microphysical processes in climate models. Based on ground-based radar observations, [Li et al. \(2019\)](#) reconstructed the long-term seasonal average “decorrelation length scale ( $L$ )” and found a significant negative correlation between this factor and the cloud fraction. Combined with the meteorological reanalysis data, a multiple regression model between  $L$  and dynamical factors was developed, with smaller biases of the cloud fraction than the previous  $L$  parameterization method. But the initial fields of numerical models can only be obtained from limited spatial grid points, and it is still difficult for climate models with a coarse resolution to achieve an accurate representation of the CWR.

In terms of the mesoscale models, most of the studies focused on moisture balance, and they have been carried out gradually from a specific single weather system to typical characteristics of cloud systems in a typical re-

gion, with models adopted from single cloud models to three-dimensional mesoscale models. Tao et al. (1993) conducted a detailed study on the moisture budget of squall line systems by using mesoscale numerical models and found that the moisture budget of squall line systems in equatorial regions differed significantly from that in midlatitudes, and this moisture budget was analyzed in terms of the effects of topography and broad weather context. Sui et al. (1994) investigated the water balance at equatorial latitudes by using global circulation models (GCMs) to discuss the advective differences in water vapor and hydrometeors at each boundary. Based on numerical simulations, Colle et al. (2005) analyzed the microphysical budget of orographic clouds on a windward slope and discussed the mechanism of each microphysical process. Braun (2006) used the Weather Model 5 (MM5) to simulate a typhoon process and explored in depth the condensation, precipitation, and water vapor budget in clouds, revealing water budget characteristics of typhoon peripheral cloud systems. Also, Zhou et al. (2010) studied the water balance and the precipitation mechanism of the primary stratiform cloud system in Henan Province by using the MM5 model, and they calculated the regional water substances. By using the Global and Regional Assimilation and Prediction System (GRAPES) model, Chen et al. (2011) analyzed the distributions of the water vapor and hydrometeors, the changes of each cloud microphysical process, and the precipitation efficiency of hydrometeors during a precipitation event in Chongqing. Based on the Weather Research and Forecasting (WRF) dynamical framework coupled with the cloud microphysics scheme developed by the Chinese Academy of Meteorological Sciences (CAMS), Tao et al. (2015) conducted a numerical simulation study on the structure and water balance of primary stratocumulus mixed clouds in Beijing, and they calculated the precipitation efficiency of hydrometeors and water substances. Moreover, Zhang et al. (2020) statistically studied the distributions of atmospheric water resources in the Liupan Mountains based on the fifth generation ECMWF atmospheric reanalysis (ERA5) data, MODIS data, and WRF models. Also, the influence of topography on the precipitation efficiency of hydrometeors was analyzed. These studies mainly focused on the simulation of single cases, while there were few studies on the characteristics of the regional long-term atmospheric hydrometeors and the CWR quantification.

For the CWR quantification, Zhou et al. (2020) used the CWR-DQ and CWR-NQ to show the CWR calculation for two typical months of spring and summer in North China. In addition, they preliminarily studied

CWR and related characteristic quantities. Nevertheless, it is a great challenge to achieve numerical simulation and quantitative estimation of the CWR for continuous years by a high-precision cloud-resolving mesoscale model with a 1–3-km resolution and minute-scale calculation steps. This model facilitates a detailed understanding of the fine-grained characteristics of the regional CWR.

Based on the WRF mesoscale model, we build a set of CWR numerical simulation and quantification modules in the CAMS scheme, i.e., CMA-CPEFS, and perform 1-yr experiments with the CWR in North China during 2017. The established numerical simulation methods and CWR simulation results are evaluated comprehensively by the conservation of atmospheric water balance, the comparisons of cloud and precipitation between simulations and observations, and comparisons of CWR characteristics between CWR-NQ and CWR-DQ. In order to better understand the CWR characteristic quantities and its potential development in North China, a preliminary analysis of the spatiotemporal characteristics of the CWR in North China is carried out based on model results.

The remainder of this paper is organized as follows. Section 2 introduces the CMA-CPEFS model and the calculation scheme of CWR characteristic quantities. In Section 3, the spatiotemporal distributions of simulated water vapor, clouds, and precipitation are compared with the observations. In Section 4, the conservation of atmospheric water substances is examined, and simulation results of CWR related characteristic quantities are compared with the diagnostic results. Section 5 provides a fine analysis of the spatiotemporal characteristics of the regional CWR.

## 2. The CMA-CPEFS cloud resolving model and CWR simulation quantification method

### 2.1 CMA-CPEFS cloud resolving model

In this study, the dynamical framework of the WRF is adopted, coupled with the CAMS cloud microphysical scheme (Gao et al., 2011). The CAMS scheme is developed from the early convective–stratiform cloud model proposed by Hu and He (1988, 1989). Forecast variables include the water content and the number concentration of cloud water, rain, ice crystals, snow, and graupel, and the cloud droplet spectrum width. In addition, 31 cloud physical processes are considered in the CAMS scheme, such as merging, condensation, cloud–rain auto-conversion, nucleation, multiplication, and freezing (Fig. 1). The description of physical processes is

mainly based on field observations and indoor experiments, and the calculation scheme is characterized by the quasi-implicit format for calculating sink terms of microphysical predictors, which ensures the stability, positive definiteness, and conservation of the calculation. Recently, the CAMS scheme has been selected for many scientific experiments, such as the study of the precipitation and water cycle in the Northwest Pacific (Gao and Sui, 2013), the analysis of cloud precipitation characteristics in the Tibetan Plateau (Gao et al., 2016), the estimation of water budget during precipitation processes in North China (Tao et al., 2015), the meteorological condition analysis of aircraft icing (Sun et al., 2021), and numerical simulation study of artificial catalysis (Liu et al., 2021). In addition, the Cloud Precipitation Explicit Forecast System, developed by coupling the CAMS cloud scheme in WRFv4.1, has been in operation since 2017, and its simulation performance has been proved to be better by a large number of cases.

## 2.2 Quantification of the CWR

### 2.2.1 Calculation of the 16 composition variables of the CWR

According to the definition and calculation algorithms of the CWR proposed by Zhou et al. (2020), the basis of the CWR quantification is the atmospheric water substance balance equations [Eq. (1)].

$$\begin{cases} M_{h1} + Q_{hi} + C_{vh} = M_{h2} + Q_{ho} + C_{hv} + P_s \\ M_{v1} + Q_{vi} + C_{hv} + E_s = M_{v2} + Q_{vo} + C_{vh}, \\ M_{w1} + Q_{wi} + E_s = M_{w2} + Q_{wo} + P_s \end{cases} \quad (1)$$

where there are 16 variables/terms related to hydrometeors (h), water vapor (v), and water substances (w) in the atmosphere, referred to as CWR compositions. The variables  $M_{x1}$  and  $M_{x2}$  ( $x$  denotes h, v, and w, the same below) indicate the mass of hydrometeors, water vapor, and water substances at the initial and end time of the study period, termed as instantaneous state variables. The variables  $Q_{xi}$  and  $Q_{xo}$  represent the inflow and outflow of hydrometeors, water vapor, and water substances during the study period, called advection variables. Cloud evaporation ( $C_{vh}$ ) is the mass of hydrometeors converted from water vapor through condensation (including desublimation), and cloud condensation ( $C_{hv}$ ) is the mass of water vapor converted from hydrometeors through evaporation (including sublimation). Combined with surface evaporation ( $E_s$ ) and surface precipitation ( $P_s$ ),  $C_{vh}$  and  $C_{hv}$  are referred to as the source and sink terms, respectively. Based on Eq. (1), we establish the CWR-NQ and use the model results to calculate the 16 CWR compositions at any time and in any region. Then, the CWR characteristics are analyzed by different variables.

Since the time interval of the model output (1 h) is far greater than the calculated time step in the model (60 s for 9-km resolution and 20 s for 3-km resolution), except the state terms, the advection and source–sink terms integrated by time steps in the model are much more accurate than the hourly model outputs.

#### (1) State terms

The variable  $M_x$  (kg) is the amount of atmospheric hydrometeors/water vapor/water substances in the study area at any time. In the numerical model, the units of variables are  $\text{kg kg}^{-1}$ , and the units become  $\text{kg m}^{-3}$  after multiplying by the air density. The mass of water vapor

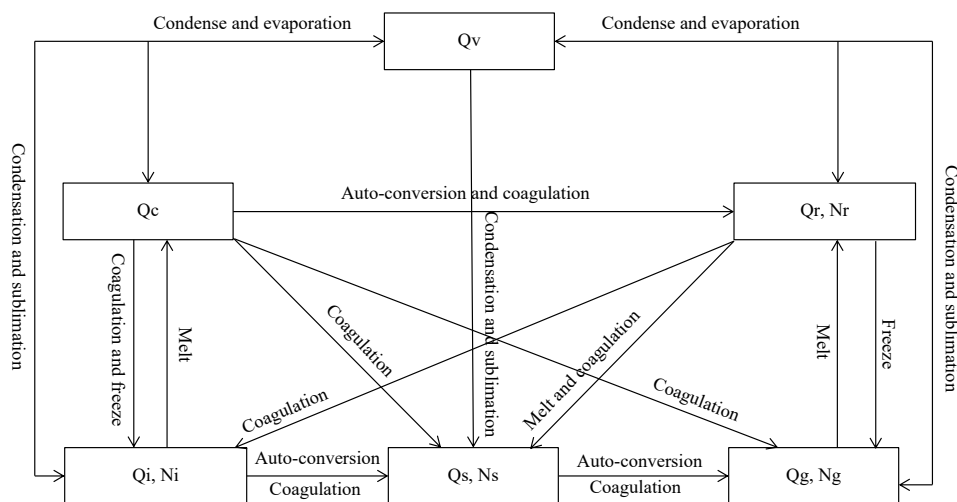


**Fig. 1.** Cloud microphysics processes of CAMS scheme. Qv, Qc, Qr, Qi, Qs, and Qg are water vapor, cloud drops, rain drops, ice crystals, snow particles, and graupel particles, respectively; Nr, Ni, Ns, and Ng are number concentration of rain drops, ice crystals, snow particles, and graupel particles, respectively.

(kg) at a single grid point can be obtained through three-dimensional integration. Atmospheric hydrometeors are the sum of cloud water, rain, ice crystals, snow, and graupel, with the unit of  $\text{kg kg}^{-1}$ , and the mass of atmospheric hydrometeors (kg) at grid points is obtained in the same way as that of water vapor.

### (2) Advection terms

The advection term is the total amount of water substances that inflow and outflow the analysis area through each horizontal boundary in a certain period. In the model, the longitudinal ( $x$ -direction) and latitudinal ( $y$ -direction) water substance fluxes are calculated at boundary  $(i - 1, i)$  and boundary  $(j - 1, j)$  by the following equations [Eqs. (2)–(3)].

$$\begin{aligned} \text{FXQ}_x &= U(i, j, k) \times [Q_x(i, j, k) \\ &\quad + Q_x(i - 1, j, k)]/2 \times \Delta y \times \Delta z \times \Delta t \times \rho, \end{aligned} \quad (2)$$

$$\begin{aligned} \text{FYQ}_x &= V(i, j, k) \times [Q_x(i, j, k) \\ &\quad + Q_x(i, j - 1, k)]/2 \times \Delta x \times \Delta z \times \Delta t \times \rho. \end{aligned} \quad (3)$$

Among them,  $\Delta x$  and  $\Delta y$  are the grid lengths,  $\Delta z$  the grid height,  $\Delta t$  the integration step, and  $\rho$  the air density. Since there are positive and negative values of  $U$  and  $V$ , fluxes at each boundary have positive and negative values. For the eastern, southern, western, and northern boundaries of a single air column, the wind direction pointing toward the study area indicates the input, and otherwise, it means the output. For example, on the western boundary, positive values represent the input, and negative values denote the output. For layer  $k$ , the input ( $Q_{xi}$ ) and output ( $Q_{xo}$ ) of the grid are obtained by summing up the input and output at the four boundaries. The total input and output of the grid column is the sum of the input and output of the grid at each layer. In terms of any rectangular region, based on the conservation law, the mass variation can be calculated by the horizontal advection at four boundaries of the study region. Based on this, the total input and output of a variable in the study region can be obtained by the sum of the input and output at the four boundaries.

### (3) Source and sink terms

The variables  $C_{vh}$  and  $C_{hv}$  at all the grids in the region are summed up to obtain the total condensation and evaporation (kg) during the study period. Both  $C_{vh}$  and  $C_{hv}$  are intermediate variables in microphysical processes, and the units are  $\text{kg kg}^{-1} \text{ s}^{-1}$ . Similar to the treatment of water vapor and hydrometeors, the total amount of  $C_{vh}$  ( $C_{hv}$ ) at each grid is obtained by multiplying the condensation (evaporation) rate by time step, density, and the grid area.

The variables  $E_s$  and  $P_s$  (kg) are the accumulated surface evaporation and precipitation in a region during the

study period, respectively. Surface evaporation (mm) and precipitation ( $\text{kg m}^2 \text{ s}^{-1}$ ) are calculated based on land surface processes and microphysical processes in the model, respectively. The mass of each horizontal grid is obtained by multiplying the surface evaporation and precipitation by the grid area ( $\Delta x \times \Delta y$ ) and integration step ( $\Delta t$ ).

### 2.2.2 Characteristic variables of the CWR

After obtaining the above 16 composition variables, the CWR and related characteristics can be quantified. The left-hand side of Eq. (1) denotes the input terms of water substances, and the right-hand side indicates the output terms. The sum of input terms is equal to that of output terms, which is the total amounts of the hydrometeors ( $GM_h$ ), total amounts of water vapor ( $GM_v$ ), and total amounts of water substances ( $GM_w$ ). For the  $GM_h$ , a part of hydrometeors that do not form surface precipitation but remain in the air are the CWR, expressed by Eq. (4).

$$\text{CWR} = GM_h - P_s. \quad (4)$$

In the study, precipitation efficiency ( $PE_x$ ) is defined as the ratio of total surface precipitation to the total amounts of hydrometeors, water vapor, and water substances. The ratio of the condensed water particles to the total water vapor is termed as condensation efficiency of water vapor ( $CE_v$ ), which is calculated by Eq. (5).

$$\begin{cases} PE_x = P_s/GM_x \\ CE_v = C_{vh}/GM_v \end{cases}. \quad (5)$$

Furthermore, the mean mass of atmospheric hydrometeors and water vapor during a certain period and the renewal time can be calculated by Eq. (6).

$$\begin{cases} MM_x = \frac{1}{N} \sum_{i=1}^{i=N} M_{xi} \\ RT_x = MM_x/(P_s/T) \end{cases}, \quad (6)$$

where  $MM_x$  denotes the state term, and  $x$  indicates  $h$ ,  $v$ , and  $w$ , i.e., atmospheric hydrometeors, water vapor, and water substances.

In summary, through continuous simulation of cloud physical processes in a certain period and region, the four-dimensional distributions of various types of atmospheric water substances and wind fields can be obtained based on the CWR-NQ. According to the calculation formulas of the CWR and physical variables, the simulation estimation of the CWR in certain regions can be realized in a specific period.

### 2.3 Scheme of numerical simulation

One of the difficulties of numerical simulation is to

ensure that the model can operate stably for a long time and that the moisture balance can be maintained in the model. When the simulations of wind fields, water vapor, clouds, and precipitation basically agree well with observations, the model results are credible.

In this study, a double-layer nested scheme is adopted, with horizontal resolutions of 9 and 3 km for the parent domain and subdomain (Fig. 2). In addition, the bi-directionality feedback between the two domains is adopted. There are 61 uneven layers in vertical direction, and the top layer is at 100 hPa. The center of the model domain is at 39.9°N, 114.5°E, and the numbers of grid points in the parent domain and subdomain are  $254 \times 182$  and  $406 \times 352$ , respectively. The initial and boundary conditions of the model are from ERA5 reanalysis data, with a resolution of  $0.25^\circ \times 0.25^\circ$ . The  $0.5^\circ \times 0.5^\circ$  sea surface temperature data are also used in the model. The underlying surface information is derived from MODIS data, with the topographic data of 30-s resolution. The simplified Arakawa–Schubert (SAS) cumulus parameterization scheme is chosen for the parent grid, which is not considered in the sub-grid. The Rapid Radiative Transfer Model (RRTM) scheme is used for longwave radiation, the Dudhia scheme for shortwave radiation, the Noah scheme for land surface processes, the Mellor–Yamada–Janjic (MYJ) scheme for boundary layer, and the MYJ Monin–Obukhov scheme for near-surface.

The simulation period is from 1200 BT (Beijing Time) 31 December 2016 to 0000 BT 1 January 2018, with a spin-up time of 12 h. During the simulation, the initial

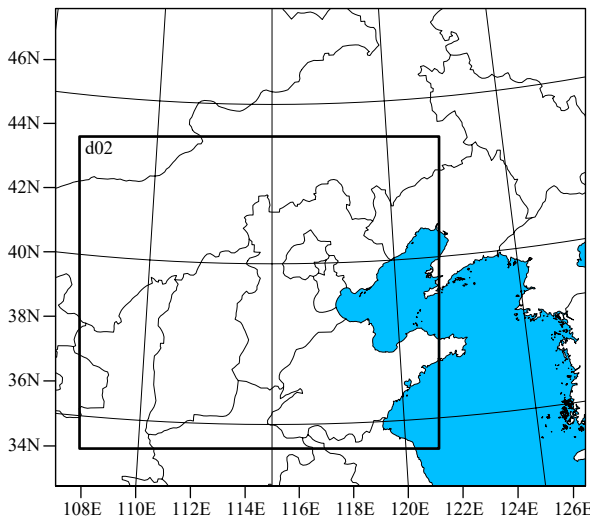


**Fig. 2.** The double nested simulation domains (the model centroids are 39.9°N and 114.5°E, the resolutions of the d01 and d02 regions are 9 and 3 km, and the boundaries of the d02 region are each scaled inward by 10 grid points for the simulated quantification region of CWR, ranging from 34° to 44°N and from 108° to 121°E).

field (1200 BT 31 December 2016) is kept constant, and the boundary conditions are updated every 6 h for a 1-yr continuous simulation. The spatial range of CWR simulation and quantification is the subdomain, i.e., North China. In order to facilitate the advection calculation, the four boundaries of the east, south, west, and north are indented inward by 10 grid points. Thus, the region of the simulation and quantification is the range of 34°–44°N, 108°–121°E.

### 3. Validation of the simulated water vapor, cloud, and precipitation

The simulations of water vapor, clouds, and precipitation are compared with observations to validate the model performance. The model results are up-scaled to a horizontal spatial resolution consistent with the observations to facilitate the comparison. Meanwhile, atmospheric hydrometeor state term, water vapor state term, and precipitation are converted to water depth (mm).

#### 3.1 Validation of the simulated clouds

The performance of the model on clouds directly determines the reasonableness of the CWR quantification results. Therefore, the simulated clouds need to be verified. The cloud fraction and cloud water path from the Clouds and the Earth's Radiant Energy System (CERES) Single Satellite Footprint (SSF) *Terra* MODIS Edition 3A cloud product (<https://ceres-tool.larc.nasa.gov/ord-tool/jsp/SYN1degEd41Selection.jsp>) are used as observations for comparison. This remote sensing product has been extensively calibrated (Dewitte and Clerbaux, 1999; Lee et al., 2000; Loeb et al., 2016), with high accuracy of the instrument measurements, reducing the uncertainties in estimations of planetary albedo and outgoing longwave radiation.

##### 3.1.1 Validation of the simulated cloud water path

CERES satellite instrument provides  $1^\circ \times 1^\circ$  inversion products of cloud liquid water path (LWP) and cloud ice water path (IWP). In the study, the model outputs include liquid cloud water and rain (as simulated LWP by vertical integration), as well as solid cloud ice, snow, and graupel (as simulated IWP by vertical integration). For the comparison with the CERES product, the simulations are up-scaled from 3-km resolution to  $1^\circ \times 1^\circ$ . Figure 3 shows the spatial distributions of the annual mean simulated LWP and IWP and the CERES product. Note that the sum of the LWP and IWP is the atmospheric hydrometeor state term. The results show that the maximum value of the annual mean LWP from the remote sensing product is about  $150 \text{ g m}^{-2}$ , which appears

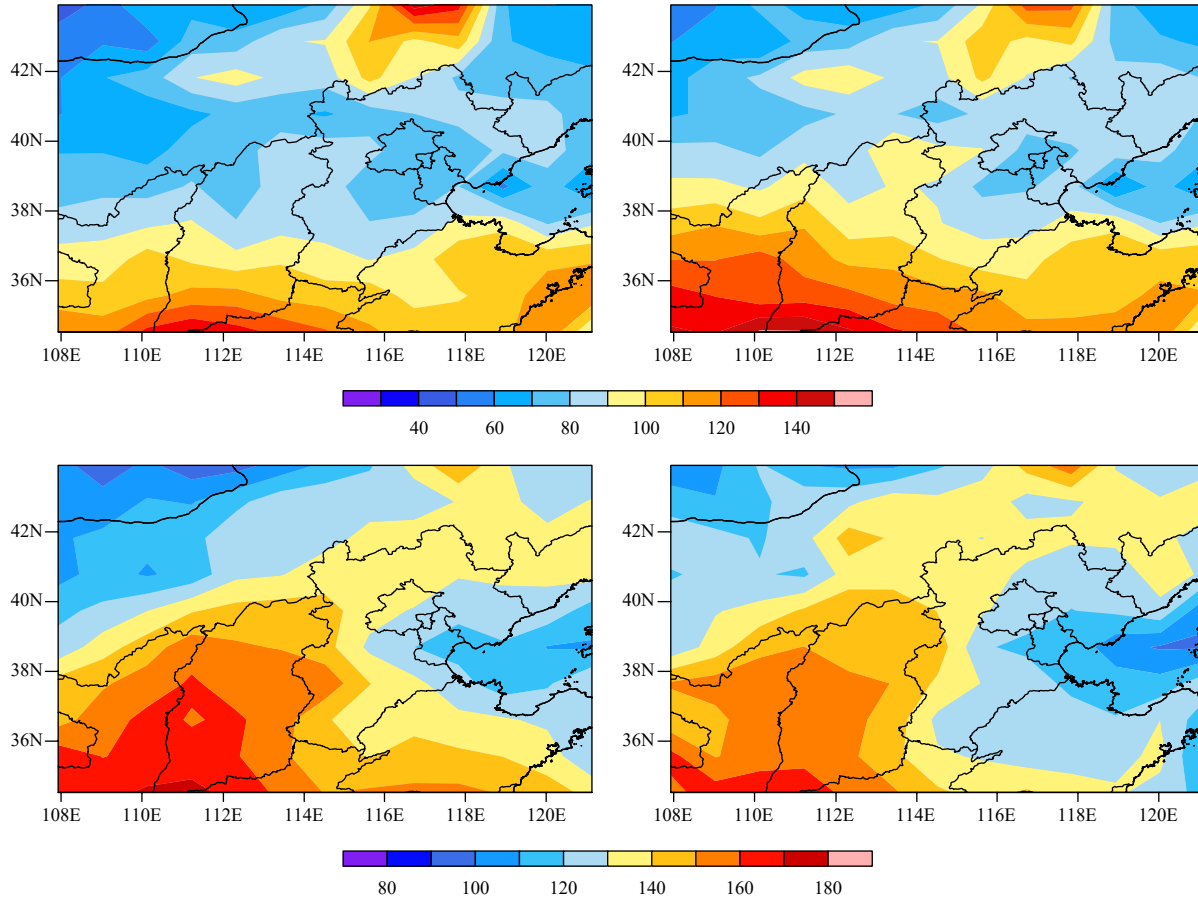


**Fig. 3.** Comparisons of simulations (left) with the observed (right) for the LWP (mm; top) and IWP (mm; bottom) over North China in 2017.

at the southwest corner of the study area. Meanwhile, there is a large-value area in the northeast of the region within Inner Mongolia. Overall, the values and spatial distribution of the simulated LWP are generally consistent with the observations. The maximum IWP value from the remote sensing product is  $180 \text{ g m}^{-2}$ , and the large-value center is also located at the southwest corner of the study area. The large-value area of the observed IWP shows a distribution extending from the southwest to the northeast. In general, the IWP simulations are generally consistent with the observations, especially for the banded high-value area. However, the values of the simulated IWP in south-central Shanxi are slightly larger than the observations.

### 3.1.2 Validation of the simulated cloud fraction

The simulations of the cloud fraction are not obtained from direct outputs of the model but are derived from the diagnosis of simulated atmospheric hydrometeor mixing ratio. All the atmospheric hydrometeor mixing ratio is summed up to calculate the total atmospheric hydrometeor mixing ratio in the grid. The thresholds for identifying clouds in previous studies are different for the different study objects, such as stratus clouds and convective

clouds, and for the different study regions, such as tropical and mid-high latitudes (Ma et al., 2009). In this study,  $0.001 \text{ g kg}^{-1}$  is chosen as the threshold for identifying cloud areas, i.e., if the water content of atmospheric hydrometeors is greater than  $0.001 \text{ g kg}^{-1}$ , clouds are considered to be present and marked as 1, and vice versa, clouds are not present and marked as 0. The probability of cloud occurrence is defined that the sum of cloud occurrences for each time in a period is divided by the total time, which has a similar physical significance to the cloud fraction from the CERES satellite product.

Figure 4 shows the distributions of the simulated and observed cloud fraction in North China for the whole year and each season in 2017. The results show that the distributions, intensities, and change trends of the simulations are similar to those of the CERES satellite product, decreasing gradually from the south to the north. The simulation results for the whole year and spring are relatively close to the observations compared with other seasons, while the simulation performance is relatively poor for winter. The cloud fraction for the whole year, spring, autumn, and winter are overestimated, while the summer simulation underestimates.

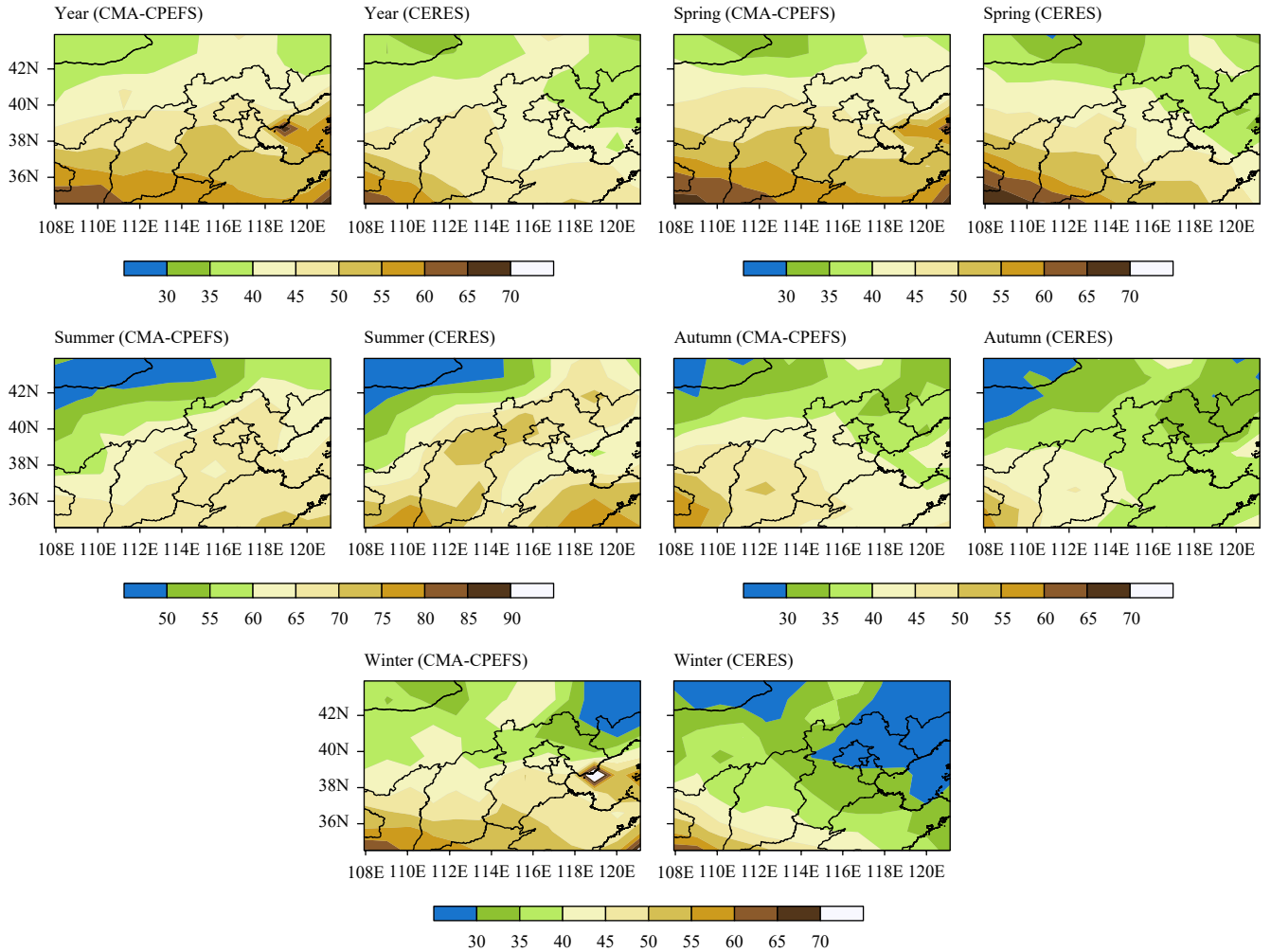


**Fig. 4.** Comparisons between the simulated (left) and observed (right) cloud fraction (%) over North China in the whole year and four seasons.

The simulated and observed cloud fraction in the study region are analyzed at the  $1^\circ \times 1^\circ$  grid by scattering comparison (Fig. 5), and the total number of grid points is 143. By statistics, we obtained the fitting results of simulations with observations in the four seasons and the whole year. Table 1 shows the correlation coefficient ( $R$ ), root-mean-square error (RMSE), and relative RMSE (RRMSE) between the simulated and observed cloud fraction for each season and the whole year. The errors show that the simulation performance is better in spring and worse in winter, with the RMSE of 0.74 (spring) and

1.76 (winter) and the RRMSE of 0.15 (spring) and 0.36 (winter). For the fitting results,  $R$  for the whole year can reach 0.79. The model performance in simulating cloud fraction is better in spring and autumn, with  $R$  of 0.72 and 0.78, respectively. It is the worst in winter, but with  $R$  also reaching 0.45. For the summer simulation,  $R$  is 0.68.

The RMSE and the fitting results show that the performance for simulating cloud fraction is good in spring, and the simulations in winter have a larger deviation compared with the observations. The simulation perform-

**Table 1.** RMSE, RRMSE, and  $R$  of the cloud fraction and annual precipitation between the simulated and the observed in  $1^\circ$  grid over North China in the whole year. The observations are from CERES (cloud) and CMORPH (Climate Prediction Center morphing technique; precipitation) product

	Cloud fraction			Total precipitation		
	RMSE	RRMSE	$R$	RMSE	RRMSE	$R$
Year	0.66	0.14	0.79	9.14	0.37	0.79
Spring	0.74	0.15	0.72	9.36	0.32	0.82
Summer	1.71	0.35	0.68	11.98	0.56	0.76
Autumn	1.36	0.28	0.78	11.91	0.55	0.76
Winter	1.76	0.36	0.45	14.23	0.68	0.56

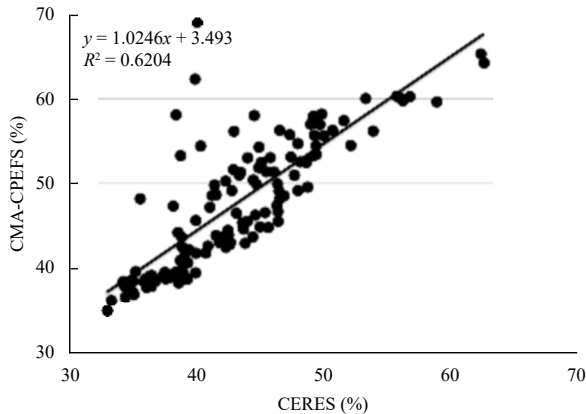


**Fig. 5.** Correlation between the simulated and observed cloud fraction in  $1^\circ$  grid over North China in the whole year.

ance for the whole year is better than that of the individual seasons in terms of both correlations and errors, with an  $R$  of 0.79, an RMSE of 0.66, and an RRMSE of 0.14. In addition, the slope of the fitting curve between simulations and observations for the whole year is close to 1.

### 3.2 Validation of the simulated water vapor

The atmospheric precipitable water product (the vertically integrated state term of water vapor) from the NCEP atmospheric reanalysis data is in correspondence to the water vapor state terms simulated in the study. The NCEP data have a temporal resolution of 6 h, i.e., 4 times a day (0000, 0600, 1200, and 1800 UTC), with a horizontal spatial resolution of  $1^\circ \times 1^\circ$  and 26 vertical layers from 1000 to 10 hPa.

The comparison between the simulated annual average water vapor and the reanalysis data is shown in Fig. 6. The magnitude, distribution, and large-value center of the simulated annual mean water vapor state term ( $MM_v$ ) are generally consistent with the annual mean value of the at-

mospheric precipitable water from the NCEP reanalysis data. Both simulation results and the reanalysis data show that the maximum value of the  $MM_v$  is about 23 mm, with the large-value center located in the southeastern part of the simulated area. The  $MM_v$  is below 9 mm in the northwestern part of the simulated area. In addition, the RMSE and RRMSE are 1.51 and 0.16 mm for the simulations in the whole year.

### 3.3 Validation of the simulated precipitation

The CMORPH satellite fusion precipitation product (China merged hourly precipitation analysis version 1.0) released by the National Meteorological Information Center is used to validate the spatial distribution of the simulated annual precipitation in North China, with a resolution of  $0.1^\circ \times 0.1^\circ$ . Based on a probability density function plus optimal interpolation, the hourly precipitation data from more than 30,000 automatic meteorological stations nationwide after quality control were fused with the CMORPH satellite-retrieved precipitation product (30-min temporal resolution and 8-km spatial resolution) developed by the U.S. Climate Prediction Center. In this way, the CMORPH satellite fusion precipitation product was generated.

The annual precipitation is obtained by accumulating the observed daily precipitation. Comparing the distribution and evolution of the simulated annual precipitation with the observations (Fig. 7), we find that the precipitation is overestimated in simulations for the whole year, spring, autumn, and winter, and it is underestimated in summer, especially for some extreme precipitation. For the model results in the whole year, the precipitation is stronger in the southeast of the study area and weaker in the northwest, and the maximum value of annual precipitation exceeds 700 mm. However, the precipitation in

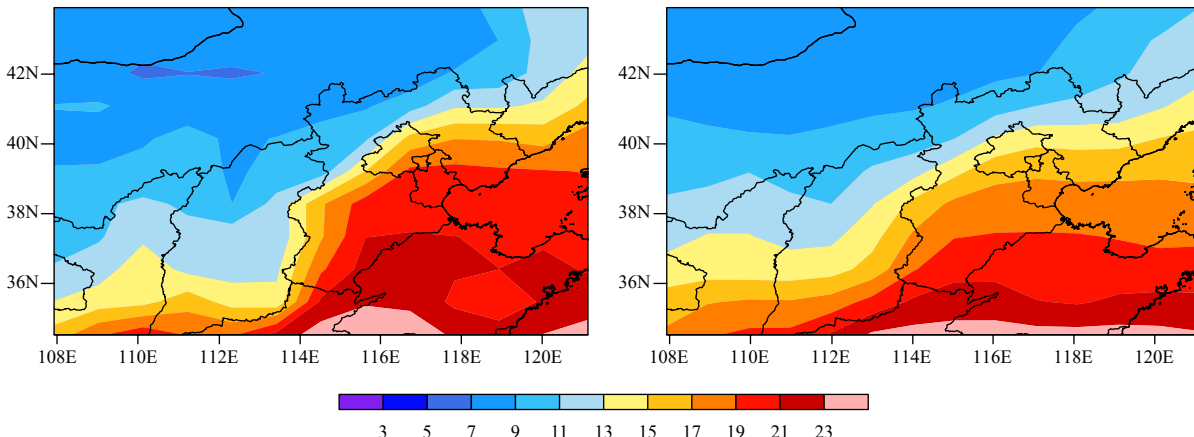


**Fig. 6.** Comparison between the simulated (left) annual mean water vapor (mm) and the NCEP reanalysis data (right) over North China in 2017.

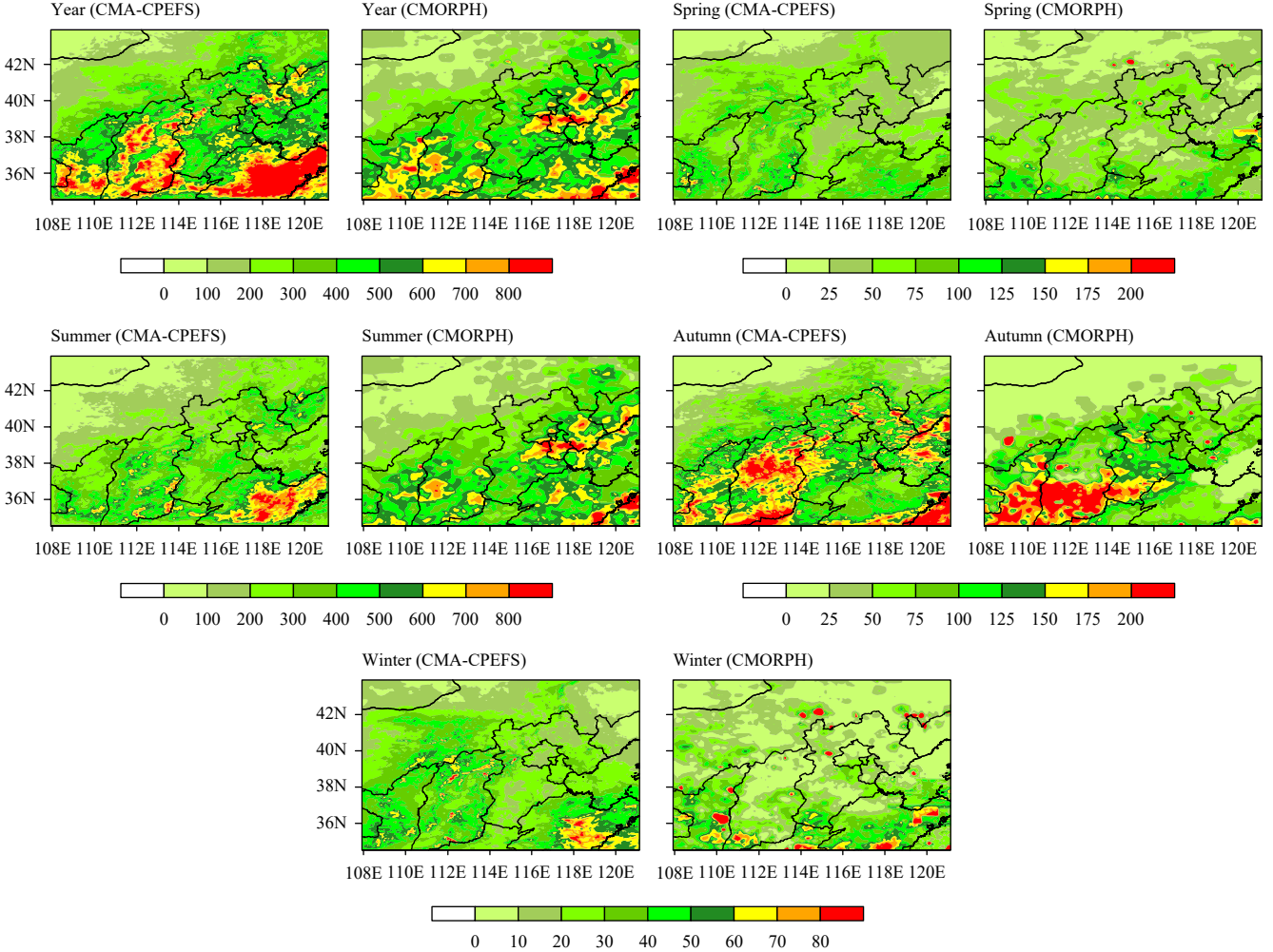


**Fig. 7.** Distributions of yearly accumulated precipitation (mm) of simulations (left) and observations (right) in 2017 (the spatial resolution of the CMORPH is  $0.1^\circ \times 0.1^\circ$ , and for comparison the simulated 3-km results are also upscaled to  $0.1^\circ$  spatial resolution). The observations are from the CMORPH product.

the southwest is significantly overestimated. The model results in summer and autumn indicate that the spatial distribution of rainbands from southwest to northeast can be represented. However, there is an underestimation over the whole study area in summer and an overestimation at the southeast corner in autumn. In winter, the simulation performance is slightly worse, especially in the western part where the precipitation is generally overestimated. The main reason for the deviation in summer is that the extreme precipitation and several critical precipitation processes are significantly underestimated, as shown from the evolution of daily precipitation shown in Fig. 8. There are two reasons for the appearance of the deviation for winter simulations. One is that the weak precipitation of less than 3 mm has empty and missing reports. The other is that errors are gradually enlarged in the later period due to the model simulation for a long time.

Similar to the comparison way of the cloud fraction,

the  $R^2$  between the simulated and observed precipitation is also calculated at the  $1^\circ \times 1^\circ$  grid (Fig. 9). The  $R$  between the simulated annual accumulative rainfall and the CMORPH product can reach 0.79. The performance for simulating precipitation is better in spring, summer, and autumn, with  $R$  of 0.82, 0.76, and 0.76, respectively. The model performance is the worst in winter, but its  $R$  also reaches 0.56. In addition, for simulations in the whole year, the RMSE and RRMSE (Table 1) are 9.14 and 0.37 mm, respectively.

The above comparisons of the clouds, water vapor, and precipitation show that the model results for the whole year are consistent with the observations, indicating that the CMA-CPEFS mesoscale cloud-resolving model and its simulation results are reasonable and reliable. Therefore, the CMA-CPEFS model can be used to calculate and analyze the CWR and related characteristic quantities.

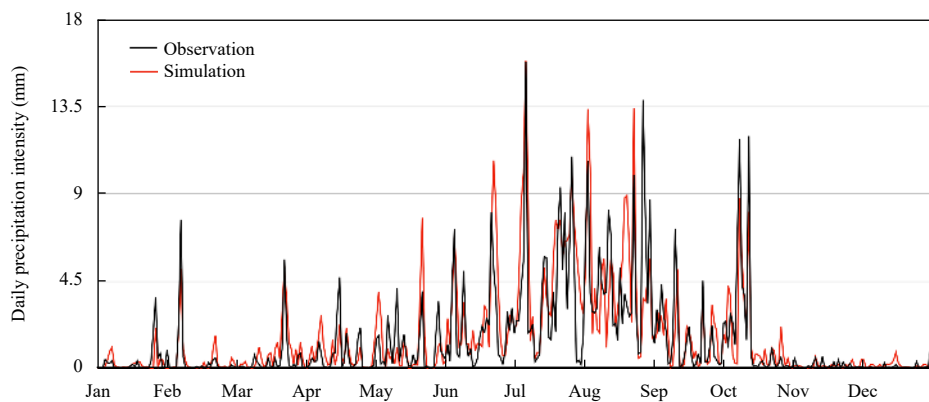


**Fig. 8.** Evolution of the simulated (red line) and observed (black line) daily precipitation in 2017. The observations are from CMORPH product.

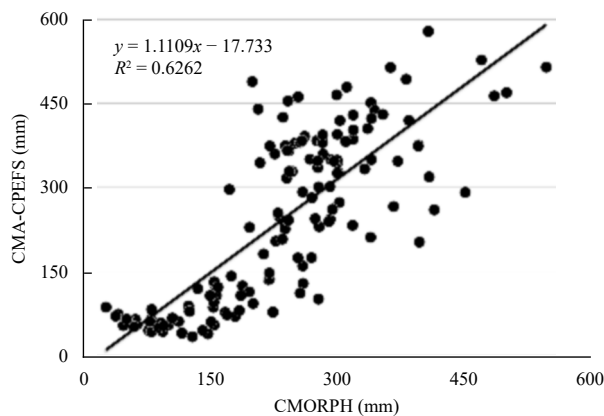


**Fig. 9.** Correlation of precipitation between the simulated and observed in 1° grid over North China in the whole year;  $x$  and  $y$  in the fitting equation represent the observations and the simulations. The observations are from CMORPH product.

#### 4. Validation of the simulated CWR and related characteristic quantities

##### 4.1 Conservation validation and general characteristic of the atmospheric water substances

###### 4.1.1 Evaluation of the atmospheric water substance conservation

The CWR compositions in North China obtained from the CWR-NQ method are listed in **Table 2**, and the conservation of water substances is verified based on the numerical simulation results. The results show that the sum

of the income term ( $M_{h1} + Q_{hi} + C_{vh}$ ) and the sum of the expenditure term ( $M_{h2} + Q_{ho} + C_{hv} + P_s$ ) of atmospheric hydrometeors are 1192.59 and 1190.03 billion tons, respectively. After 1-yr continuous simulation, the remaining term is 2.55 billion tons, equivalent to 0.2% of the total atmospheric hydrometeors. In terms of water substances, the sum of the income term ( $M_{w1} + Q_{wi} + E_s$ ) and the sum of the expenditure term ( $M_{w2} + Q_{wo} + P_s$ ) are 6938.86 and 6944.34 billion tons, respectively, and the remaining term is -5.48 billion tons, equivalent to 0.08% of the total atmospheric water substances.

###### 4.1.2 Basic characteristics of the atmospheric water balance in North China

The differences between income and expenditure terms (**Table 2**) suggest that the annual water substance convergence in North China is negative (-27 mm), and the surface evaporation is greater than the precipitation (22 mm). Thus, North China is an arid region where the precipitation (540 mm) is mainly provided by net condensation (524 mm).

The amount of water substance state is about 3 mm, less than 1% of the annual precipitation. The change magnitude of the annual water substances is about 0.2% of the precipitation, accounting for a small proportion in the annual water balance. The amount of hydrometeors state is about 0.03 mm, which is 1% of water substances and counts for a quite small proportion.

**Table 2.** CWR compositions in North China obtained by the CWR-NQ method

Income term	Regional total ( $10^{11}$ kg)	Water content of unit air column (mm)	Expenditure term	Regional total ( $10^{11}$ kg)	Water content of unit air column (mm)	Balance (mm)
$M_{w1}$	50.30	3.9	$M_{w2}$	38.66	3.0	0.9
$Q_{wi}$	62,145	4855	$Q_{wo}$	62,491	4882	-27
$E_s$	7193	562	$P_s$	6913	540	22
$M_{h1}$	0.3	0.03	$M_{h2}$	0.3	0.02	0.01
$Q_{hi}$	2369	185	$Q_{ho}$	2146	168	17
$C_{vh}$	9555	746	$C_{hv}$	2841	222	524

#### 4.2 Comparison between the CWR-NQ and CWR-DQ

In addition to the CWR-NQ, Zhou et al. (2020) established a CWR-DQ based on satellite observations of clouds, atmospheric reanalysis data, and surface precipitation observations, and they made the CWR diagnosis for the period of 2017 and the region of 34°–44°N, 108°–121°E, which is the same as that of this study. For the diagnostic quantification, the water vapor and wind data are directly derived from the NCEP atmospheric reanalysis data. The cloud data are obtained from the temperature and humidity diagnosis by using the NCEP reanalysis data. In addition, the precipitation data are derived from the Global Precipitation Climatology Project (GPCP) data (Cai et al., 2020). Based on the above data, the daily diagnostic results of cloud water are calculated, with a  $1^\circ \times 1^\circ$  horizontal spatial resolution.

Based on these grid products, the monthly CWR quantification results over North China can be obtained by integration over a specific period. Since the CWR quantification during a long period in the region has not been carried out in previous studies, the CWR simulations are compared with the observation diagnosis results in the study. Also, the correlation between the simulations and observations is analyzed as supporting evidence for the reasonableness of the simulations.

Figure 10 shows the scatterplots of the monthly average water vapor state and monthly precipitation in North China in 2017 for model results and diagnostic results. The determination coefficients of the water vapor state and the precipitation obtained by the two methods reach 0.99, which means that the simulation results and diagnostic results have a good correlation.

The monthly simulations of other CWR compositions in North China are further compared with the diagnostic results, and the fitting equations and determination coef-

ficients are shown in Table 3. Overall, the monthly diagnostic results and the simulations have an excellent correlation for the monthly input and output of atmospheric hydrometeors ( $Q_{hi}$  and  $Q_{ho}$ ), the condensation and net condensation ( $C_{vh}$  and  $C_{vh} - C_{hv}$ ), the monthly average water vapor state, the monthly input and output of water vapor ( $Q_{vi}$  and  $Q_{vo}$ ), as well as the surface evaporation and precipitation ( $E_s$  and  $P_s$ ). The determination coefficients for the diagnostic and simulated results of the compositions are generally greater than 0.8, and even condensation, net condensation, input and output of water vapor, as well as surface evaporation have determination coefficients of greater than 0.9. Note that the model results are generally slightly larger than the diagnostic results.

For the CWR quantification in North China in 2017, the results of the advection, source and sink, CWR, and related characteristic quantities from the two quantification methods are listed in Table 4. The difference ( $\Delta$ ) of the quantification results between the two different methods is calculated by the following equation [Eq. (7)].

$$\text{Difference } (\Delta) = [(CWR\text{-DQ} - CWR\text{-NQ}) / CWR\text{-DQ}] \times 100. \quad (7)$$

Among the 16 CWR compositions, the water vapor advection and its total amount, surface evaporation and precipitation, net condensation, and total atmospheric water substances have deviations of less than 5%. The main difference lies in cloud condensation ( $C_{hv}$ ) and cloud evaporation ( $C_{vh}$ ), of which the differences are 27% for cloud condensation and 232% for cloud evaporation. However, the difference of net condensation is less than 1%.

(1) For the advection term, the calculation is mainly based on the dynamic field (i.e.,  $u$  and  $v$ ) and state terms of water vapor and hydrometeors which are constant with

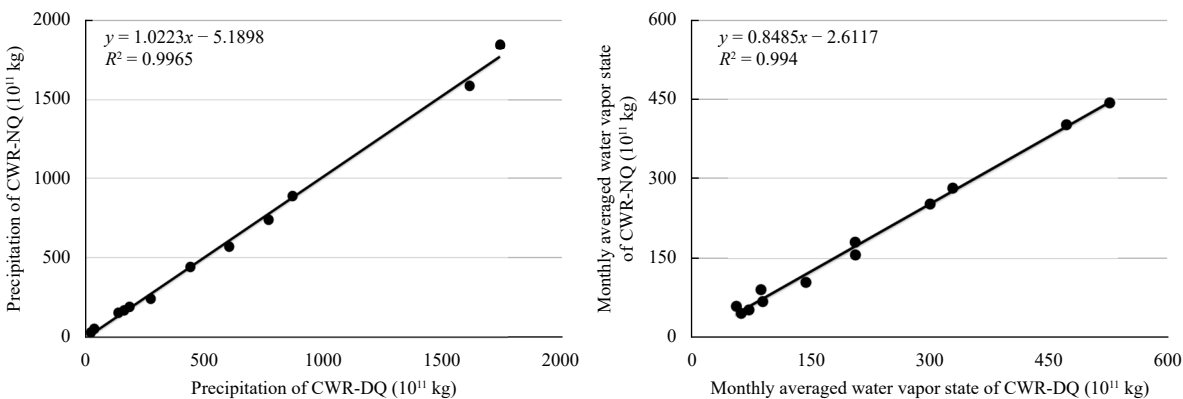


**Fig. 10.** Scatterplots and fitting curves between CWR-NQ and CWR-DQ for monthly precipitation (left) and monthly average water vapor state (right) in North China.

**Table 3.** Correlations of the daily CWR compositions in 2017 between the CWR-NQ and CWR-DQ;  $x$  and  $y$  in the fitting equations represent the observational diagnostic results and model results

	Fitting equation	$R^2$
$Q_{hi}$	$y = 0.7060x + 39.491$	0.82
$Q_{ho}$	$y = 0.8592x + 10.866$	0.88
$C_{vh}$	$y = 0.7093x + 0.0177$	0.94
$C_{vh} - C_{hv}$	$y = 0.9648x + 14.427$	0.99
$Q_{vi}$	$y = 0.9278x + 324.85$	0.92
$Q_{vo}$	$y = 0.9171x + 361.79$	0.94
$E_s$	$y = 0.9393x + 15.836$	0.93

**Table 4.** The quantification of CWR and related characteristic quantities based on the diagnostic and simulated results ( $10^{11}$  kg). The variable  $Q_{vx}$  is water vapor state terms and  $Q_{hx}$  is atmospheric hydrometeors state terms

	CWR-NQ	CWR-DQ	Difference ( $\Delta$ )
$Q_{vx}$	50.00	57.20	12.6%
$Q_{hx}$	0.32	0.51	40.0%
$Q_{hi}$	2368.84	2146.31	-10.4%
$Q_{ho}$	2146.37	1974.64	-8.69%
$Q_{vi}$	55,936.76	59,361.00	6.18%
$Q_{vo}$	60,339.79	59,686.40	-1.1%
$C_{vh}$	9555.49	7506.04	-27.3%
$C_{hv}$	2841.30	855.21	-232.2%
$C_{vh} - C_{hv}$	6714.18	6650.83	-0.95%
$E_s$	7192.93	6946.10	-3.55%
$P_s$	6913.35	6823.44	-1.32%
CWR	5011.34	2830.56	-77.04%
$GM_h$	11,924.70	9654.01	-23.52%
$GM_v$	69,568.78	67,234.60	-3.47%
$GM_w$	69,387.68	68,527.30	-1.26%
$PE_h$	57.98	70.68	17.97%
$PE_v$	9.89	10.15	2.56%
$CE_v$	13.68	11.16	-22.58%
$RT_h$	4.09	5.62	27.22%
$RT_v$	9.37	11.46	18.24%

the reanalysis data. The diagnostic results of observations are directly derived from the reanalysis data. Hence, the difference of the advection term between the results calculated by the two methods is slight.

(2) For the condensation term, the residual difference in the equilibrium of hydrometeors in the air column is treated as the net condensation during the diagnosis. The positive value of net condensation means condensation, and the negative value represents evaporation. Thus, the condensation and evaporation are underestimated without considering the difference between evaporation and condensation in the air column. Compared with simulations, the difference of the underestimated condensation and evaporation in the diagnostic results is roughly equal to about 200 billion tons. Due to the different bases, the percentages of the underestimations differ significantly, 27% for the condensation and 232% for evaporation. This situation results in the reduction of 200 billion tons

of the total water vapor, total hydrometeors, and the CWR, and the corresponding differences are -4%, -23%, and -77%. Further, it leads to increases of 3% and 18% in precipitation efficiencies of water vapor and hydrometeors. In addition, the underestimated average state terms cause 18% and 27% longer update cycles.

(3) For the surface evaporation, the diagnostic results are based on the residual term of the equilibrium equation due to the lack of reliable underlying surface information, which also causes a certain bias.

## 5. Regional characteristics of the CWR

### 5.1 Temporal features of the regional CWR

The integral dimension of each CWR composition is different. Thus, there is no spatiotemporal additivity. Theoretically, the advection term is obtained by integration along the boundary. In a large region with multiple grids, the inputs and outputs cancel each other at the inner boundary, except the outer boundary. Therefore, the input and output values cannot be integrated with space, and their importance decreases with the expansion of the region. The state term is the spatial volume integral of water vapor and hydrometeors at a certain moment, which is an instantaneous quantity and cannot be integrated over time. Thus, the importance of state terms decreases with time. The sink terms can be integrated with spatiotemporal dimensions, and they could be more significant with the increase of time and area.

In order to further understand the importance of state terms over time, August 2017, a month with relatively more precipitation, is selected to analyze the contribution of each composition to the total atmospheric hydrometeors and CWR based on the daily atmospheric moisture balance. Then, the characteristics of the monthly atmospheric moisture balance and the changes in the contribution of each composition are analyzed at monthly scale.

For the short-term CWR assessment (left panel, Fig. 11), i.e., daily scale, the source–sink terms  $C_{vh}$  and  $P_s$  are dominant factors, with contributions to total atmospheric hydrometeors ranging from 15% to 97% (mean 78%) and from 12% to 81% (mean 53%) over 31 assessment days, respectively. Meanwhile, the atmospheric hydrometeor state also contributes to the total atmospheric hydrometeors and the CWR. The ratio of  $M_h$  to  $GM_h$  exceeds 10% for most of the 31 assessment days, with a maximum value of 32%. The contribution and influence of the atmospheric hydrometeors state to the daily CWR cannot be ignored.

In terms of the long-term CWR assessment (right

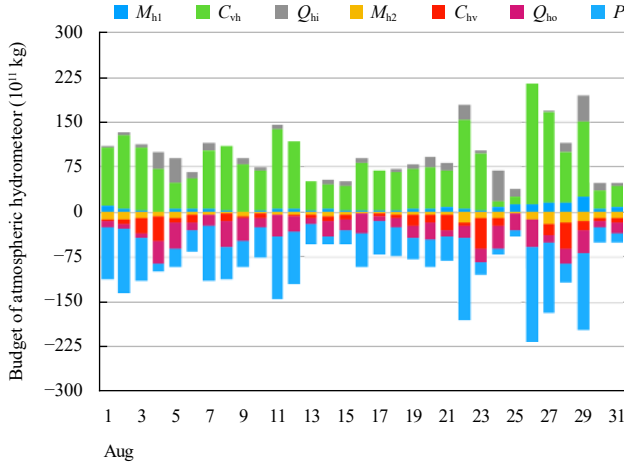


**Fig. 11.** Daily simulations in August 2017 and monthly simulations in 2017 for atmosphere hydrometeor compositions in North China.

panel, Fig. 11), i.e., monthly scale, the largest contribution to total atmospheric hydrometeors and the CWR is still from the source–sink terms. The  $C_{vh}$  and  $P_s$  generally count for more than 60% of the  $GM_h$  in the 12 assessment months. The percentage of the advection term is relatively small, with values of 20%–30%. The contribution of state term is the smallest, with a percentage basically below 0.1%, which is negligible.

For the CWR quantification at a short timescale, the effect of state terms cannot be ignored. As time increases, the effects of the advection and source–sink terms become more significant. Moreover, as the region expands, the advection terms within the region cancel each other. Only inputs and outputs along the boundary remain to play a role. Due to the accumulated source–sink effect with the expansion of the region, the influence of advection terms gradually decreases, while the impact of the source–sink terms gradually increases.

Equation (8) can be obtained from Eq. (1). Among

them,  $Q_{xi} - Q_{xo}$  is the convergence term,  $C_{vh} - C_{hv}$  the net condensation, and  $M_{x1} - M_{x2}$  the variation term of state quantities. These terms are featured by their spatiotemporal additivity, and they have positive and negative values.

$$\begin{cases} (Q_{hi} - Q_{ho}) + (C_{vh} - C_{hv}) = (M_{h2} - M_{h1}) + P_s \\ (Q_{vi} - Q_{vo}) + E_s = (M_{v2} - M_{v1}) + (C_{vh} - C_{hv}). \\ (Q_{wi} - Q_{wo}) + E_s = (M_{w2} - M_{w1}) + P_s \end{cases} \quad (8)$$

For the hydrometeors, the sum of the convergence term and net condensation is equal to the sum of the changes in the state of the hydrometeors and precipitation. The weight of the changes in state term decreases with increasing time. Meanwhile, the weight of the hydrometeor convergence term is small compared with the net condensation and precipitation. Therefore, the precipitation and the condensation show a strong positive correlation over a relatively long period (as shown in Fig. 12).

In terms of the water vapor, the sum of the conver-

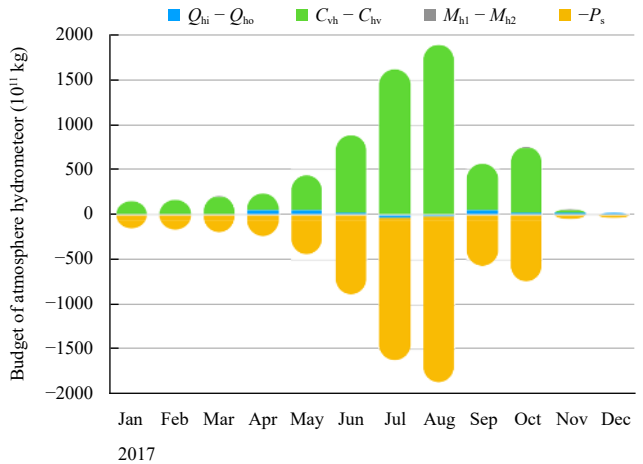
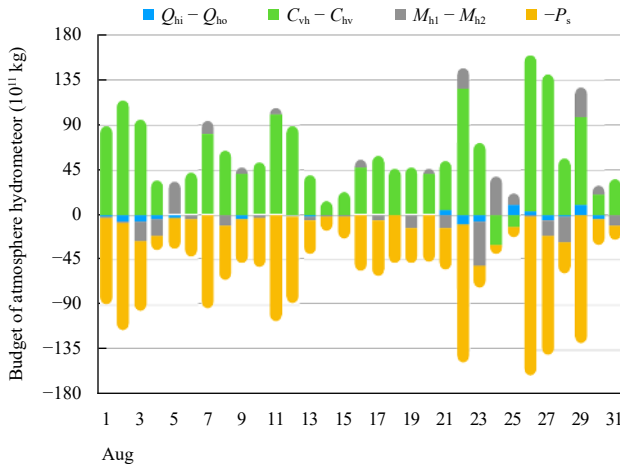


**Fig. 12.** Relationship of daily (August 2017) and monthly (2017) atmosphere hydrometeor compositions in North China.

gence and the surface evaporation is equal to the sum of the changes in the water vapor state and net condensation. Similar to hydrometeors, the effect of the water vapor state terms also decreases gradually with increasing time. Due to the magnitude difference between the base of water vapor and hydrometeors, the effect of the convergence term cannot be neglected, and its magnitude is comparable to that of net condensation. Therefore, the convergence and condensation of water vapor show a strong positive correlation in a long period (as shown in Fig. 13).

In a long period (one month), the precipitation and the condensation are positively correlated, and the condensation is positively correlated with the water vapor convergence. Thus, the precipitation and the water vapor convergence have a positive correlation. In a short period (one day), the correlation feature is similar to that of the long period. However, there are several minor differences in details. For example, during 3–5 August, the water vapor convergence was strong on 3 August, partly condensing and partly wetting the atmosphere. Condensation partly produced precipitation and partly increased the hydrometeor state, which is a distinctive pre-precipitation feature. On 4 August, the water vapor convergence gradually decreased, and all of it was condensed. Part of the condensed water vapor produced precipitation, and part of it continued to increase the hydrometeor state, which is the feature in the middle period of precipitation. By 5 August, the convergence and condensation of water vapor were weak, but precipitation was strong due to the significant reduction in hydrometeors state, which is the feature in the end period of precipitation. In terms of the case on 23–24 August, the water vapor convergence was strong on 23 August, similar to what happened on 3–5 August, partly condensing and partly wetting the at-

mosphere. Part of the condensed water vapor produced precipitation, and part of it increased the amount of hydrometeors state. On 24 August, the precipitation was kept weak, but negative condensation (i.e., evaporation) occurred, while the water vapor divergence occurred on that day. This situation indicated that most of the hydrometeors produced by the water vapor convergence on 23 August were not eventually converted into precipitation as usually happens but evaporated directly.

Therefore, at monthly scale, water vapor convergence is approximately equal to condensation, and condensation is approximately equal to precipitation. Hence, precipitation is mainly caused by water vapor convergence. At daily scale, precipitation generation by water vapor convergence cannot be completed in one step. There is a lag of about one day in this process, and this lag mainly depends on the state quantity of water vapor and hydrometeors to regulate the transition. Thus, the role of the state terms cannot be ignored at a short timescale.

## 5.2 Spatial features of the regional CWR

CWR compositions such as state terms, precipitation, surface evaporation, condensation, and evaporation are constant at different spatial scales for both total and unit area averages in the region (see Table 5), but there are huge differences in advection terms because  $Q_{xi}$  is integrated only on the boundaries. When the region is extended, only the advection term on the regional boundaries needs to be calculated, and the advection within the region can be omitted. Therefore, the values of the advection term are far smaller than the sum of  $Q_{xi}$  that is integrated at all grid points. It is worth noting that the convergence terms of water vapor and water condensate (i.e., input – output) are scale-independent, but they have positive and negative values, and the sum of area and time

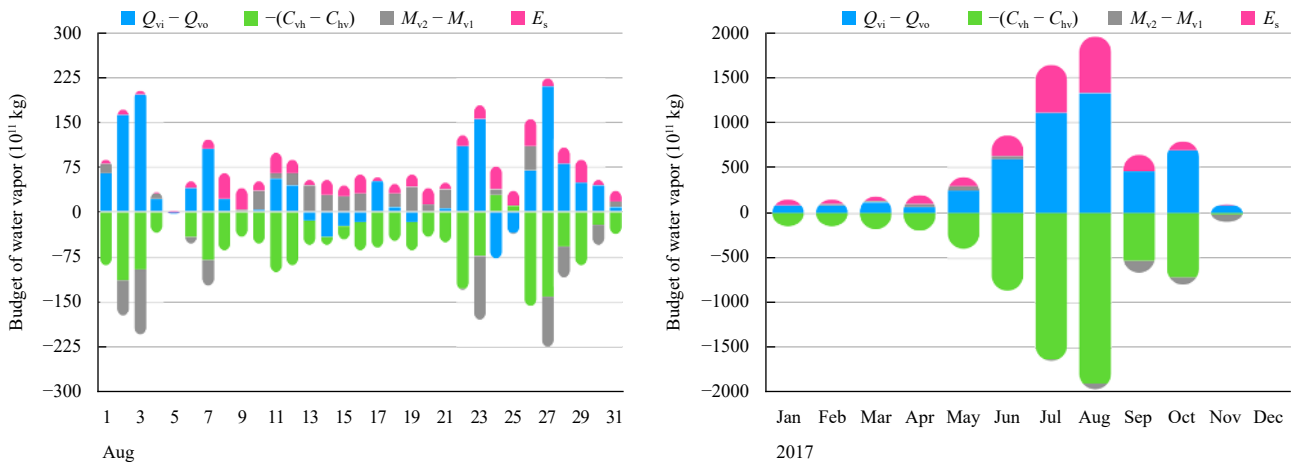


Fig. 13. As in Fig. 12, but for water vapor.

**Table 5.** Effects of grid-scales on the compositions and the characteristics of CWR (mm). The variable  $D_v$  is water vapor irradiation and  $D_h$  is atmospheric hydrometeors irradiation

Variable	3 km	1°	All region
MM <sub>v</sub>	3.9	3.9	3.9
MM <sub>h</sub>	0.025	0.025	0.025
$Q_{vi}$	519,592	34,872	4370
$Q_{vo}$	519,936	35,216	4714
$D_v$	-344	-344	-344
$Q_{hi}$	21,645	1443	185
$Q_{ho}$	21,662	1427	168
$D_h$	17	17	17
$P_s$	540	540	540
$E_s$	562	562	562
$C_{vh}$	747	747	747
$C_{hv}$	222	222	222
GM <sub>v</sub>	520,665	35,935	5435
GM <sub>h</sub>	22,390	2190	932
CWR	21,850	1650	392
PE <sub>v</sub>	0.1%	1.5%	9.9%
PE <sub>h</sub>	2.4%	24.5%	57.8%
RT <sub>v</sub> (day)	9.4	9.4	9.4
RT <sub>h</sub> (h)	4.1	4.1	4.1

will offset each other, and the effect of the difference in spatial scale of input/output can be avoided when using the form of Eq. (8) to study. A larger spatial scale may be more representative as a resource, but a smaller spatial scale is important for the study of atmospheric hydrometeor and CWR and related characteristic quantities.

Figure 14 presents the spatial distribution of the annual quantification of the CWR and related characteristic quantities in North China in 2017. The results show that the precipitation and the condensation have a high correlation, i.e., regions with larger condensation have larger annual precipitation. Also, the precipitation and the condensation have a good agreement in spatial distribution and magnitude. The annual average hydrometeors correspond well to the precipitation and the condensation. The distribution of hydrometeor renewal time shows that regions with greater precipitation have relatively shorter hydrometeor renewal time, while regions with less precipitation have a longer hydrometeor renewal time. The shortest renewal time is about 5 h, and the longest one is over 18 h.

Moreover, based on the grid with a 3-km resolution, the effect of topographic conditions (Taihang Mountains) on the CWR and related characteristic quantities is significant. The elevation drops rapidly on the east side of the mountain with altitudes of more than 2000 m. Both the precipitation and the condensation show a trend of rapid enhancement with the increasing elevation. On the west side, the elevation declines gently, and the precipitation and the condensation do not increase with the increasing

elevation. However, the precipitation and the condensation are relatively strong on both sides, with larger local precipitation, high precipitation efficiency, and a short renewal time. It can be concluded that due to the mountainous action, the local condensation is stronger than that over the plain terrain, easy to the formation of topographic clouds. This situation can induce stronger precipitation, with high precipitation efficiency and a short renewal time, resulting in the CWR in the mountains being relatively weak.

## 6. Summary

In the study, a numerical model is established based on the CAMS scheme and the concepts of CWR related characteristic quantities. The hourly simulation results of the CWR and related characteristic quantities (3-km resolution) are obtained by continuous simulation in North China in 2017. The main conclusions are as follows.

(1) In terms of the magnitudes and spatial distributions, the simulated annual mean cloud fraction, LWP, and IWP are consistent with that of the CERES satellite-retrieved product, the simulated water vapor state agrees well with the atmospheric precipitable water from NCEP reanalysis data, and the simulated annual precipitation is reasonable compared with the CMORPH satellite fused precipitation product. The time series of the simulated daily precipitation basically coincide with the observations, and the simulated cloud fraction and precipitation for the whole year and four seasons have a good correlation with the observations at 1° × 1° grid points, with a relatively small RMSE and an RRMSE.

(2) By 1-yr continuous simulation, the atmospheric moisture balance in the region basically reaches equilibrium, and the CWR-NQ can be continuously simulated for a long time with stable conservation. The general results of the CWR from numerical simulations and observational diagnosis are in good agreement, with significant positive correlations for the CWR compositions such as hydrometeor input, condensation, and surface evaporation, and their correlation coefficients exceeding 0.9. The main differences between simulations and observations lie in condensation and evaporation. However, the deviation of the net condensation is less than 1%.

(3) Also, the temporal characteristics of the CWR in North China are studied. The water vapor and hydrometeors state terms make little contribution to the water balance at monthly and annual scales and a certain contribution at hourly and daily scales. At monthly and annual scales, the water vapor convergence and the precipitation are highly positively correlated, while at hourly and

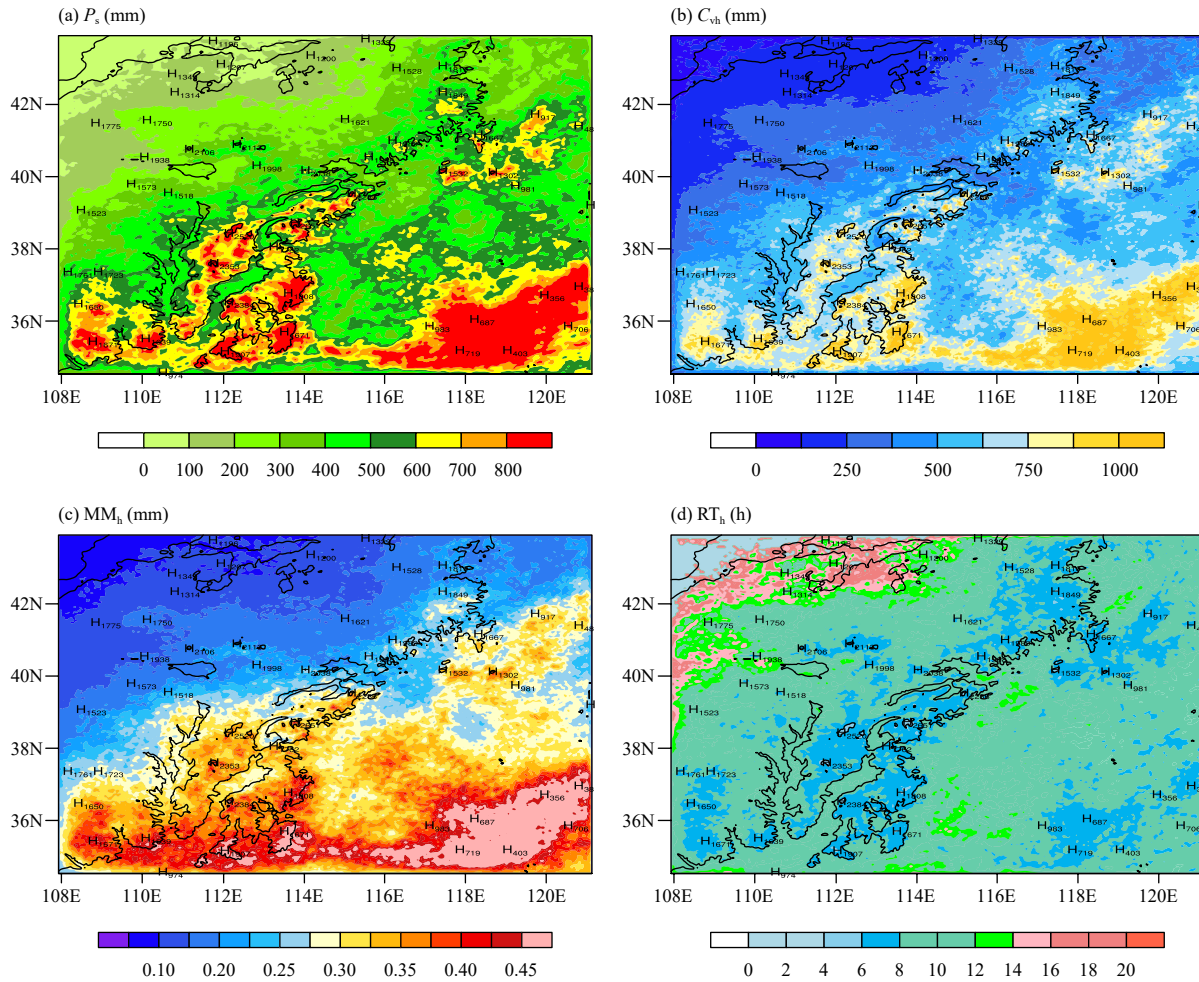


**Fig. 14.** Spatial distributions of the (a) annual precipitation, (b) cloud condensation, (c) annual mean hydrometeor state, and (d) renewal time in North China in 2017. Contour lines and numbers indicate altitudes.

daily scales, there is a certain lag between the water vapor convergence and the precipitation. The reason for this situation is that except part of the converged water vapor condensing into hydrometeors, part of it is used for wetting the atmosphere to increase the amount of the state quantities of the water vapor and hydrometeors. Therefore, the effect of the state quantities cannot be neglected at the short timescale.

(4) The spatial characteristics of the CWR in North China show that the advection terms have large variation at different spatial scales, resulting in significant differences in the total hydrometeors, the CWR, and the precipitation efficiency on scales of 3 km,  $1^\circ \times 1^\circ$ , and in the whole North China. The CWR, as a climatic feature, is more appropriate for characterizing water vapor over a region on scales above  $1^\circ \times 1^\circ$ . If the study region is overly small, the transit water substances are dominant. In addition, the topographic conditions have a certain influence on the CWR and related characteristic quantities.

In this paper, a CWR-NQ method is established, and preliminary tests show that the numerical model and its results are basically reasonable. Based on this method, fine resolution quantification results of the regional CWR for one continuous year can be calculated, which provides a reliable numerical model product for better understanding the regional CWR characteristics and improving the potential development of the artificial rainfall. The model is a complete loop system that can directly output the CWR characteristics, such as condensation and evaporation that are back-calculated through balance equations in the diagnostic method. As a result, if the comparison between the observations (such as precipitation) from the diagnostic method and the simulation from the model shows that the model results are reasonable, a further comparison of condensation and evaporation between the model results and the diagnostic results can be applied. The two methods can be validated, complement and support each other, which can

provide a more accurate diagnostic product for the climate assessment and the CWR analysis in China and the globe.

## REFERENCES

- Braun, S. A., 2006: High-resolution simulation of Hurricane Bonnie (1998). Part II: Water budget. *J. Atmos. Sci.*, **63**, 43–64, doi: [10.1175/JAS3609.1](https://doi.org/10.1175/JAS3609.1).
- Cai, M., Y. Q. Zhou, J. Z. Liu, et al., 2020: Quantifying the cloud water resource: Methods based on observational diagnosis and cloud model simulation. *J. Meteor. Res.*, **34**, 1256–1270, doi: [10.1007/s13351-020-9126-6](https://doi.org/10.1007/s13351-020-9126-6).
- Chen, X. M., Q. Zou, and K. Li, 2011: Numerical simulation analysis of rainfall characteristics and artificial precipitation potentiality in a summer precipitation process of Chongqing. *Meteor. Mon.*, **37**, 1070–1080. (in Chinese)
- Colle, B. A., M. F. Garvert, J. B. Wolfe, et al., 2005: The 13–14 December 2001 IMPROVE-2 event. Part III: Simulated microphysical budgets and sensitivity studies. *J. Atmos. Sci.*, **62**, 3535–3558, doi: [10.1175/JAS3552.1](https://doi.org/10.1175/JAS3552.1).
- Dewitte, S., and N. Clerbaux, 1999: First experience with GERB ground segment processing software: Validation with CERES PFM data. *Adv. Space Res.*, **24**, 925–929, doi: [10.1016/S0273-1177\(99\)00357-9](https://doi.org/10.1016/S0273-1177(99)00357-9).
- Gao, W. H., and C.-H. Sui, 2013: A modeling analysis of rainfall and water cycle by the cloud-resolving WRF model over the western North Pacific. *Adv. Atmos. Sci.*, **30**, 1695–1711, doi: [10.1007/s00376-013-2288-8](https://doi.org/10.1007/s00376-013-2288-8).
- Gao, W. H., F. S. Zhao, Z. J. Hu, et al., 2011: A two-moment bulk microphysics coupled with a mesoscale model WRF: Model description and first results. *Adv. Atmos. Sci.*, **28**, 1184–1200, doi: [10.1007/s00376-010-0087-z](https://doi.org/10.1007/s00376-010-0087-z).
- Gao, W. H., C.-H. Sui, J. W. Fan, et al., 2016: A study of cloud microphysics and precipitation over the Tibetan Plateau by radar observations and cloud-resolving model simulations. *J. Geophys. Res. Atmos.*, **121**, 13,735–13,752, doi: [10.1002/2015JD024196](https://doi.org/10.1002/2015JD024196).
- Hobbs, P. V., M. K. Politovich, and L. F. Radke, 1980: The structures of summer convective clouds in eastern Montana. I: Natural clouds. *J. Appl. Meteor.*, **19**, 645–663, doi: [10.1175/1520-0450\(1980\)019<0645:TSOSCC>2.0.CO;2](https://doi.org/10.1175/1520-0450(1980)019<0645:TSOSCC>2.0.CO;2).
- Hu, Z. J., and G. F. He, 1988: Numerical simulation of microphysical processes in cumulonimbus—Part I: Microphysical model. *Acta Meteor. Sinica*, **2**, 471–489.
- Hu, Z. J., and G. F. He, 1989: Numerical simulation of microphysical processes in cumulonimbus—Part II: Case studies of shower, hailstorm and torrential rain. *Acta Meteor. Sinica*, **3**, 185–199.
- Jiang, J. H., H. Su, C. X. Zhai, et al., 2012: Evaluation of cloud and water vapor simulations in CMIP5 climate models using NASA “A-Train” satellite observations. *J. Geophys. Res. Atmos.*, **117**, D14105, doi: [10.1029/2011JD017237](https://doi.org/10.1029/2011JD017237).
- Lee, R. B., III, K. J. Priestley, B. R. Barkstrom, et al., 2000: Terra spacecraft CERES flight model 1 and 2 sensor measurement precisions: Ground-to-flight determinations. Proceedings of SPIE 4135, Earth Observing Systems V, SPIE, San Diego, CA, United States, 1–12, doi: [10.1117/12.494216](https://doi.org/10.1117/12.494216).
- Li, J. M., B. D. Jian, C. F. Zhao, et al., 2019: Atmospheric instability dominates the long-term variation of cloud vertical overlap over the Southern Great Plains site. *J. Geophys. Res. Atmos.*, **124**, 9691–9701, doi: [10.1029/2019JD030954](https://doi.org/10.1029/2019JD030954).
- Liu, W. G., Y. Tao, Y. Q. Zhou, et al., 2021: Simulation of stratiform cloud seeding, its rainfall enhancement effect and mechanism study based on a real trajectory of aircraft. *Acta Meteor. Sinica*, **79**, 340–358, doi: [10.11676/qxxb2021.011](https://doi.org/10.11676/qxxb2021.011). (in Chinese)
- Loeb, N. G., N. Manalo-Smith, W. Y. Su, et al., 2016: CERES top-of-atmosphere earth radiation budget climate data record: Accounting for in-orbit changes in instrument calibration. *Remote Sens.*, **8**, 182, doi: [10.3390/rs8030182](https://doi.org/10.3390/rs8030182).
- Ma, Z. S., Q. J. Liu, Y. Y. Qin, et al., 2009: Verification of forecasting efficiency to cloud microphysical characters of meso-scale numerical model for artificial rainfall enhancement by using TRMM satellite data. *Acta Meteor. Sinica*, **67**, 260–271, doi: [10.3321/j.issn:0577-6619.2009.02.009](https://doi.org/10.3321/j.issn:0577-6619.2009.02.009). (in Chinese)
- Mason, B. J., 1971: *The Physics of Clouds*. 2nd ed. Oxford University Press, Oxford, UK, 688 pp.
- Pruppacher, H. R., and J. D. Klett, 1978: *Microphysics of Clouds and Precipitation*. Springer, Dordrecht, 714 pp, doi: [10.1007/978-94-009-9905-3](https://doi.org/10.1007/978-94-009-9905-3).
- Ramanathan, V., R. D. Cess, E. F. Harrison, et al., 1989: Cloud-radiative forcing and climate: Results from the Earth Radiation Budget Experiment. *Science*, **243**, 57–63, doi: [10.1126/science.243.4887.57](https://doi.org/10.1126/science.243.4887.57).
- Song, Y. J., F. L. Qiao, Z. Y. Song, et al., 2013: Water vapor transport and cross-equatorial flow over the Asian-Australia monsoon region simulated by CMIP5 climate models. *Adv. Atmos. Sci.*, **30**, 726–738, doi: [10.1007/s00376-012-2148-y](https://doi.org/10.1007/s00376-012-2148-y).
- Sui, C. H., K. M. Lau, W. K. Tao, et al., 1994: The tropical water and energy cycles in a cumulus ensemble model. Part I: Equilibrium climate. *J. Atmos. Sci.*, **51**, 711–728, doi: [10.1175/1520-0469\(1994\)051<0711:TTWAEC>2.0.CO;2](https://doi.org/10.1175/1520-0469(1994)051<0711:TTWAEC>2.0.CO;2).
- Sun, J., C. Tan, Y. Q. Zhou, et al., 2021: Meteorological conditions of two cases of aircraft icing in spring in Xinjiang. *Meteor. Environ. Sci.*, **44**, 24–32, doi: [10.16765/j.cnki.1673-7148.2021.04.004](https://doi.org/10.16765/j.cnki.1673-7148.2021.04.004). (in Chinese)
- Tao, W.-K., J. Simpson, C. H. Sui, et al., 1993: Heating, moisture, and water budgets of tropical and midlatitude squall lines: Comparisons and sensitivity to longwave radiation. *J. Atmos. Sci.*, **50**, 673–690, doi: [10.1175/1520-0469\(1993\)050<0673:HMAWBO>2.0.CO;2](https://doi.org/10.1175/1520-0469(1993)050<0673:HMAWBO>2.0.CO;2).
- Tao, Y., J. X. Li, J. Dang, et al., 2015: A numerical study on precipitation process and moisture budget of stratiform and embedded convective cloud over Beijing area. *Chinese J. Atmos. Sci.*, **39**, 445–460, doi: [10.3878/j.issn.1006-9895.1412.13209](https://doi.org/10.3878/j.issn.1006-9895.1412.13209). (in Chinese)
- Yang, Y. K., C. F. Zhao, and H. Fan, 2020: Spatiotemporal distributions of cloud properties over China based on Himawari-8 advanced Himawari imager data. *Atmos. Res.*, **240**, 104927, doi: [10.1016/j.atmosres.2020.104927](https://doi.org/10.1016/j.atmosres.2020.104927).
- Zhang, P., Z. Y. Yao, S. Jia, et al., 2020: Study of the characteristics of atmospheric water resources and hydrometeor precipitation efficiency over the Liupan Shan area. *Chinese J. Atmos. Sci.*, **44**, 421–434, doi: [10.3878/j.issn.1006-9895.1904.19104](https://doi.org/10.3878/j.issn.1006-9895.1904.19104). (in Chinese)
- Zhao, C. F., S. C. Xie, S. A. Klein, et al., 2012: Toward under-

- standing of differences in current cloud retrievals of ARM ground-based measurements. *J. Geophys. Res. Atmos.*, **117**, D10206, doi: [10.1029/2011JD016792](https://doi.org/10.1029/2011JD016792).
- Zhao, C. F., Y. Y. Chen, J. M. Li, et al., 2019: Fifteen-year statistical analysis of cloud characteristics over China using Terra and Aqua Moderate Resolution Imaging Spectroradiometer observations. *Int. J. Climatol.*, **39**, 2612–2629, doi: [10.1002/joc.5975](https://doi.org/10.1002/joc.5975).
- Zhou, F. F., Y. C. Hong, and Z. Zhao, 2010: A numerical study of the moisture budget and the mechanism for precipitation for a stratiform cloud system. *Acta Meteor. Sinica*, **68**, 182–194, doi: [10.11676/qxb2010.019](https://doi.org/10.11676/qxb2010.019). (in Chinese)
- Zhou, Y. Q., M. Cai, C. Tan, et al., 2020: Quantifying the cloud water resource: Basic concepts and characteristics. *J. Meteor. Res.*, **34**, 1242–1255, doi: [10.1007/s13351-020-9125-7](https://doi.org/10.1007/s13351-020-9125-7).

Tech & Copy Editor: Qi WANG